Research in Astronomy and Astrophysics, 24:075014 (9pp), 2024 July https://doi.org/10.1088/1674-4527/ad539b

Observation of Complex Organic Molecules Containing Peptide-like Bonds Toward Hot Core G358.93–0.03 MM1

Arijit Manna and Sabyasachi Pal
Department of Physics and Astronomy, Midnapore City College, Paschim Medinipur, West Bengal, 721129, India; amanna.astro@gmail.com, sabya.pal@gmail.com

Received 2024 April 26; revised 2024 May 31; accepted 2024 June 1; published 2024 July 8

Abstract

In star formation regions, the complex organic molecules (COMs) that contain peptide bonds (–NH–C(=O)–) play a major role in the metabolic process because –NH–C(=O)– is connected to amino acids (R-CHNH$_2$–COOH). Over the past few decades, many COMs containing peptide-like bonds have been detected in hot molecular cores (HMCs), hot corinos, and cold molecular clouds, however, their prebiotic chemistry is poorly understood. We present the first detection of the rotational emission lines of formamide (NH$_2$CHO) and isocyanic acid (HNCO), which contain peptide-like bonds toward the chemically rich HMC G358.93–0.03 MM1, using high-resolution and high-sensitivity Atacama Large Millimeter/submillimeter Array bands 6 and 7. We estimate that the column densities of NH$_2$CHO and HNCO toward G358.93–0.03 MM1 are $(2.80 \pm 0.29) \times 10^{15}$ cm^{-2} and $(1.80 \pm 0.42) \times 10^{16}$ cm^{-2} with excitation temperatures of 165 ± 21 K and 170 ± 32 K, respectively. The fractional abundances of NH$_2$CHO and HNCO toward G358.93–0.03 MM1 are $(9.03 \pm 1.44) \times 10^{-10}$ and $(5.80 \pm 2.09) \times 10^{-9}$. We compare the estimated abundances of NH$_2$CHO and HNCO with the existing three-phase warm-up chemical model abundance values and notice that the observed and modeled abundances are very close. We conclude that NH$_2$CHO is produced by the reaction of NH$_2$ and H$_2$CO in the gas phase toward G358.93–0.03 MM1. Likewise, HNCO is produced on the surface of grains by the reaction of NH and CO toward G358.93–0.03 MM1. We also find that NH$_2$CHO and HNCO are chemically linked toward G358.93–0.03 MM1.

Key words: ISM: individual objects (G358.93–0.03) – ISM: abundances – ISM: kinematics and dynamics – stars: formation – astrochemistry

1. Introduction

In complex organic molecules (hereafter COMs), the peptide bond [–NH–C(=O)–] links two amino acids to produce proteins. So, those COMs with peptide bonds provide information regarding the origin of life in the universe. In the interstellar medium (ISM), formamide (NH$_2$CHO), cyanamide (NH$_2$CN), isocyanic acid (HNCO), and acetamide (CH$_3$CONH$_2$) are COMs containing peptide-like bonds. NH$_2$CHO has an amide–amide bond (–N–C(=O)–), which is crucial for the synthesis of proteins. NH$_2$CHO contains carbon (C), hydrogen (H), oxygen (O), and nitrogen (N), which are important for biological systems. NH$_2$CHO also acts as a prebiotic precursor of genetic and metabolic materials (Saladino et al. 2012). The dipole moment of NH$_2$CHO is $\mu_a = 3.61$ Debye and $\mu_b = 0.852$ Debye (Kurland & Wilson 1957). The emission lines of NH$_2$CHO were first detected in high-mass star formation regions Sgr B2 and Orion KL (Rubin et al. 1971). The evidence of NH$_2$CHO was also found in several high- and low-mass star formation regions (Bisschop et al. 2007; Adande et al. 2013; Kahane et al. 2013; López-Sepulcre et al. 2015; Manna et al. 2024), extragalactic sources (Muller et al. 2013), comets (Bockelée-Morvan et al. 2000; Biver et al. 2014; Goesmann et al. 2015), and shocked regions (Yamaguchi et al. 2012; Mendoza et al. 2014).

In the ISM, isocyanic acid (HNCO) is the simplest organic molecule, consisting of four biogenic elements, C, H, O, and N, all of which are present in living bodies. HNCO also acts as a precursor of several prebiotic COMs, including those molecules linked with astrochemical and astrobiological interest, such as amino acids, nucleobases, and sugars (Fedoseev et al. 2015; Gorai et al. 2020). Laboratory experiments suggested that CH$_4$ and HNCO can produce peptide-bonded molecules in the solid state (Ligterink et al. 2018). HNCO is a prolate asymmetric top molecule, and its rotational levels exhibit hyperfine splitting owing to the nuclear spin of nitrogen (Niedenhoff et al. 1995; Lapinov et al. 2007). The dipole moment of HNCO is $\mu_a = 1.60$ Debye and $\mu_b = 1.35$ Debye (Kukolich et al. 1971). The evidence of HNCO was first found toward Sgr B2 (Snyder & Buhl 1972; Churchwell et al. 1986; Kuan & Snyder 1996). Additionally, evidence of HNCO has also been found toward hot cores and hot corinos (Blake et al. 1987; van Dishoeck et al. 1995; MacDonald et al. 1996; Bisschop et al. 2008; Gorai et al. 2020; Canelo et al. 2021), galactic molecular clouds (Jackson et al. 1984; Zinchenko et al. 2000), and translucent clouds (Turner et al. 1999). Although there were many chemical modeling works to investigate the evolution of NH_2CHO and HNCO, the formation pathways of both molecules remain unclear (Gorai et al. 2020).

The most chemically rich objects in the ISM are the hot molecular cores (hereafter HMCs) (Bisschop et al. 2007; Belloche et al. 2013; Manna & Pal 2022a, 2022b; Manna et al. 2023). HMCs represent the early phases of high-mass star-forming regions. The typical masses of HMCs are $\geqslant 100\,M_{\odot}$, which indicates that HMCs are reservoirs of several types of COMs, including precursors of NH_2CH_2COOH (van Dishoeck & Blake 1998). Our current idea regarding high-mass star formation regions is incomplete due to a lack of a sufficient number of observations of this kind of source. Recent observational studies indicate the evolution of high-mass star-forming regions as follows: infrared dark clouds (IRDCs) → HMCs → hyper/ultra-compact H II regions → H II regions, which are surrounded by ionized high-mass stars (Beuther et al. 2007). The middle stages between the IRDCs and ultracompact H II regions are known as the HMCs. Owing to the lack of ultraviolet (UV) photons, the temperatures of the central protostars in the HMCs rise because of the increase in the temperatures of the dust and gaseous material. In ISM, HMCs have a high gas density ($n_{\rm H_2} \geqslant 10^6$ cm^{-3}), a warm temperature ($\geqslant$100 K), and a compact and small source size ($\leqslant$0.1 pc) (van Dishoeck & Blake 1998; Williams & Viti 2014). Previous molecular line surveys at millimeter and submillimeter wavelengths show that several types of COMs like CH_3OH, CH_3OCHO, CH_3OCH_3, CH_3CN, and C_2H_5CN are frequently found in different HMCs because of the high temperature and evaporation of H_2O and organic ice mantles (Herbst & van Dishoeck 2009, and references therein).

G358.93–0.03 (R.A.: $17^{\rm h}43^{\rm m}10\overset{\rm s}{.}02$, decl.: $-29^{\circ}51'45\overset{''}{.}8$) is the massive star-forming region that is located $6.75^{+0.37}_{-0.68}$ kpc from Earth (Reid et al. 2014; Brogan et al. 2019). There are eight submillimeter continuum sources in G3589.93–0.03, which have been designated from G3589.93–0.03 MM1 to G3589.93–0.03 MM8 in decreasing R.A. (Brogan et al. 2019). The luminosity and mass of G358.93–0.03 are $\sim 7.7\times10^3\,L_{\odot}$ and $167\pm12\,M_{\odot}$, respectively (Brogan et al. 2019). Two of the eight sources, G358.93–0.03 MM1 (hereafter MM1) and G358.93–0.03 MM3 (hereafter MM3), have been confirmed as line-rich HMCs (Brogan et al. 2019; Bayandina et al. 2022). Earlier, maser lines of CH_3OH, $^{13}CH_3OH$, HNCO, and HDO were detected toward MM1 using the Atacama Large Millimeter/submillimeter Array (ALMA), Tianma Radio Telescope (TMRT), and Very Large Array facilities (Brogan et al. 2019; Chen et al. 2020). Except for the maser lines, Brogan et al. (2019) also detected the emission lines of CH_3CN from MM1 and MM3, but they do not estimate the abundance of this molecule. The emission lines of NH_2CN, the simplest sugar-like molecule CH_2OHCHO, and the anti-freeze molecule $(CH_2OH)_2$, and possible NH_2CH_2COOH precursor molecule CH_3NH_2 were also detected toward MM1 using the ALMA bands 6 and 7 (Manna & Pal 2023, 2024; Manna et al. 2023, 2024). The detection of the above-mentioned molecules indicates that the MM1 is an ideal candidate for studying the emission lines of different types of complex biomolecules, including biologically relevant molecules.

In this paper, we report the first detection of the emission lines of NH_2CHO and HNCO toward the HMC MM1 with ALMA. The gas temperature and column density of NH_2CHO and HNCO were estimated using the local thermodynamic equilibrium (LTE) model. We also address the probable formation pathways of NH_2CHO and HNCO toward MM1. The observations and data analysis are shown in Section 2. The results of the emission line detection of NH_2CHO and HNCO are provided in Section 3. The discussion and conclusions are presented in Sections 4 and 5 respectively.

2. Observation and Data Reductions

We used openly available raw data of the massive star-forming region G358.93–0.03, observed with the ALMA 12 m array with bands 6 and 7 (which span the frequency ranges of 290.51–306.01 GHz and 225.44–242.06 GHz) (PI: Crystal Brogan). The band 6 observation was performed in four spectral windows with frequency ranges of 225.44–226.38 GHz, 229.48–229.72 GHz, 240.26–241.20 GHz, and 241.12–242.06 GHz. Similarly, the band 7 observation was performed in four spectral windows with frequency ranges of 290.51–292.39 GHz, 292.49–294.37 GHz, 302.62–304.49 GHz, and 304.14–306.01 GHz. The ALMA bands 6 and 7 observations were conducted on 2019 April 16 and 2019 November 11, with on-source integration times of 3265.92 and 756.0 s respectively. The star formation region G358.93–0.03's phase center was $(\alpha, \delta)_{\rm J2000}$ = 17:43:10.000, –29:51:46.000. To observe G358.93–0.03 in ALMA band 6, 45 antennas were set up with a minimum baseline of 15.1 m and a maximum baseline of 740.4 m. To observe G358.93–0.03 for ALMA band 7, 47 antennas were set up with a minimum baseline of 14 m and a maximum baseline of 2517 m. The bandpass and flux calibrators for bands 6 and 7 during the observations were J1924–2914 and J1550+0527, respectively, whereas the phase calibrator for bands 6 and 7 was J1744–3116.

We employed the Common Astronomy Software Application (CASA 5.4.1) with an ALMA data analysis pipeline for data reduction and imaging (McMullin et al. 2007). We utilized the Perley–Butler 2017 flux calibrator model with the SETJY task for flux calibration (Perley & Butler 2017). After flagging the bad antenna data, we subsequently constructed the flux and bandpass calibration using pipeline tasks HIFA_BANDPASSFLAG and HIFA_FLAGDATA. We separated the target data with all available rest frequencies using the CASA task MSTRANSFORM after gain calibration. Utilizing the CASA task TCLEAN with line-free channels, we constructed a continuum emission image of G358.93–0.03. The continuum emission image of G358.93–0.03 at a frequency of 303.39 GHz is shown in Figure 1. Utilizing these data, Manna et al. (2023) recently

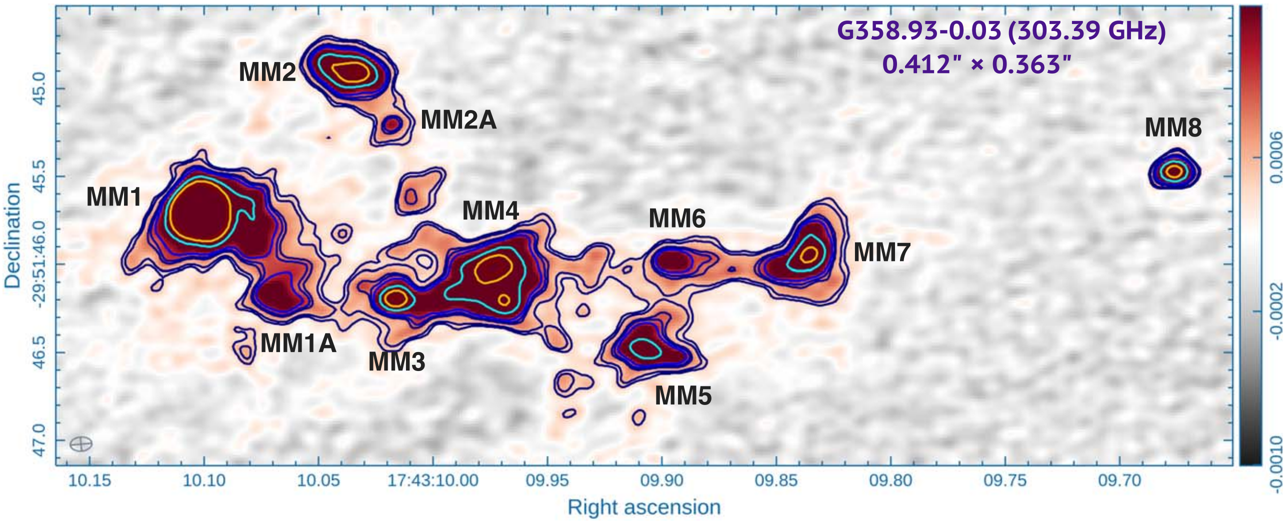

Figure 1. Millimeter wavelength continuum emission image of massive star formation region G358.93–0.03 at a frequency of 303.39 GHz. The synthesized beam size of the image is $0''.41 \times 0''.36$. The contour levels start at 2.5σ and increase by a factor of $\sqrt{2}$.

investigated in detail the dust continuum emissions from G358.93–0.03 (see Figure 1 in Manna et al. 2023). In addition to eight sources, Manna et al. (2023) also discovered two additional sources associated with MM1 and MM2, which are referred to as MM1A and MM2A respectively. Thus, in this study, we did not address the continuum emission characteristics of G358.93–0.03. Next, we employ the UVCONTSUB task to remove the continuum emission from the UV plane of the calibrated data. After that, to produce spectral data cubes of G358.93–0.03, we used the CASA task `TCLEAN` with the SPECMODE = CUBE parameter and Briggs weighting at a robust value of 0.5. Finally, we corrected the primary beam pattern in continuum images and spectral data cubes using the `IMPBCOR` task.

3. Result

3.1. Molecular Lines in G358.93–0.03

In the spectral data cubes of G358.93–0.03, we observed molecular line emissions from hot cores MM1 and MM3. We did not find any molecular line emissions from other sources in G358.93–0.03. The synthesized beam sizes of the spectral data cubes of G358.93–0.03 at ALMA band 6 were $0''.55 \times 0''.45$, $0''.53 \times 0''.46$, $0''.52 \times 0''.42$, and $0''.51 \times 0''.42$. Similarly, the synthesized beam sizes of the spectral data cubes at ALMA band 7 were $0''.42 \times 0''.36$, $0''.42 \times 0''.37$, $0''.41 \times 0''.36$, and $0''.41 \times 0''.35$, respectively. The molecular spectra were extracted by drawing a $0''.90$ diameter circular region over the MM1 and MM3, which is greater than the line emitting regions of both hot cores. The pointing center of MM1 is α (J2000) = $17^{h}43^{m}10^{s}.101$, δ (J2000) = $-29°51'45''.693$. Similarly, the pointing center of MM3 is α (J2000) = $17^{h}43^{m}10^{s}.0144$, δ (J2000) = $-29°51'46''.193$. Recently, Manna et al. (2023) used this band 7 data, and they claimed that MM1 is more chemically rich than MM3. In the band 7 molecular spectra of MM1, Manna et al. (2023) noticed an inverse P-Cygni profile in the emission lines of CH_3OH. That indicates MM1 is undergoing an infall. Manna et al. (2023) did not see any inverse P-Cygni profile in the emission lines of CH_3OH toward MM3. The velocities of the spectra (V_{LSR}) of MM1 and MM3 are -16.5 km s^{-1} and -18.2 km s^{-1}, respectively (Manna et al. 2023, Manna & Pal 2024). From the chemically rich spectra, we focused only on studying the emission lines of COMs that contain peptide-like bonds, which are discussed in the following sections.

3.2. Rotational Emission Lines NH_2CHO Toward MM1

We employed the LTE model with the Cologne Database for Molecular Spectroscopy (CDMS) and Jet Population Laboratory (JPL) molecular databases to find the rotational emission lines of NH_2CHO from the chemically rich molecular spectra of MM1 (Pickett et al. 1998; Müller et al. 2005). For fitting the LTE spectral model over the observed emission lines of NH_2CHO, we employed the Markov Chain Monte Carlo (MCMC)[1] algorithm in the CASSIS software package (Vastel et al. 2015). The gas density of the inner region of MM1 is 2×10^{7} cm^{-3}, indicating that the LTE assumptions are true for this source (Stecklum et al. 2021). Through analyzing the molecular spectra using the LTE model, we have detected four rotational emission lines of the complex N- and O-bearing molecule NH_2CHO toward MM1. The upper state energies of the detected emission lines of NH_2CHO varied between 113

---

[1] https://cassis.irap.omp.eu/docs/CassisScriptingDoc/computation/mcmc_method.html#mcmc-method

and 275.80 K. After detecting the emission lines of NH_2CHO, we obtained the molecular transitions, upper state energy (E_u) in K, Einstein coefficients (A_{ij}) in s^{-1}, line intensity ($S\mu^2$) in Debye^2, full-width at half maximum (FWHM) in $km\,s^{-1}$, optical depth (τ), and integrated intensities ($\int T_{mb}dV$) in $K\,km\,s^{-1}$. The LTE fitting spectral lines of NH_2CHO are shown in Figure 2 and the corresponding spectral parameters are listed in Table 1. Except for NH_2CHO, we also fitted the rest of the 250 molecular transitions, which were taken from CDMS and JPL molecular databases, across the observed spectra of MM1 to better understand the blending effect. After spectral analysis, we noticed that all detected lines of NH_2CHO are non-blended, and all transition lines exhibit $\geqslant 4\sigma$ statistical significance. The best-fit column density of NH_2CHO is $(2.80 \pm 0.29) \times 10^{15}\,cm^{-2}$ with an excitation temperature of 165 ± 21 K, which was estimated based on LTE modeling. The estimated excitation temperature of NH_2CHO suggests this molecule originates from the warm inner region of MM1 because the gas temperature of the warm inner region of the HMCs is above 100 K (van Dishoeck & Blake 1998; Williams & Viti 2014). The abundance of NH_2CHO toward MM1 with respect to molecular H_2 is $(9.03 \pm 1.44) \times 10^{-10}$, where the column density of molecular H_2 toward MM1 is $(3.10 \pm 0.2) \times 10^{24}\,cm^{-2}$ (Manna et al. 2023).

3.3. Rotational Emission Lines of HNCO Toward MM1

Using the LTE-modeled spectra, we detected seven rotational emission lines of HNCO toward MM1 using the ALMA bands 6 and 7. The upper-state energies (E_u) of the identified rotational emission lines of HNCO vary between 69.62 and 720.30 K. After spectral analysis, we noticed that the emission line of HNCO at a frequency of 241.498 GHz ($J = 11$ (4,7)–10(4,6)) is blended with CHDCO. All other detected transitions are non-blended. The non-blended emission lines of HNCO exhibited $\geqslant 4.5\sigma$ statistical significance. The resultant LTE-fitted spectral line and spectral line parameters of HNCO are shown in Figure 2 and Table 1. The best-fit column density of HNCO is $(1.80 \pm 0.42) \times 10^{16}\,cm^{-2}$ with an excitation temperature of 170 ± 32 K, which was estimated based on LTE modeling. The abundance of HNCO with respect to molecular H_2 toward the MM1 is $(5.80 \pm 2.09) \times 10^{-9}$, where the column density of molecular H_2 toward the MM1 is $(3.10 \pm 0.2) \times 10^{24}\,cm^{-2}$ (Manna et al. 2023).

3.4. Searching the Emission Lines of NH_2CHO and HNCO Toward MM3

After the detection of the rotational emission lines of NH_2CHO and HNCO toward MM1, we used the LTE-modeled spectra to search for these molecules toward MM3. However, we were unable to find the emission lines of those molecules toward MM3. As per the LTE analysis, the upper limit column densities of NH_2CHO and HNCO toward MM3 are $\leqslant (2.05 \pm 0.85) \times 10^{13}\,cm^{-2}$ and $\leqslant (8.12 \pm 1.26) \times 10^{14}\,cm^{-2}$, respectively. The upper limit of the abundances of NH_2CHO and HNCO toward MM3 are $\leqslant (5.84 \pm 1.26) \times 10^{-11}$ and $\leqslant (2.31 \pm 1.27) \times 10^{-9}$ respectively, where the column density of molecular H_2 toward the MM3 is $(3.51 \pm 0.7) \times 10^{23}\,cm^{-2}$ (Manna et al. 2023).

3.5. Spatial Distribution of NH_2CHO and HNCO Toward MM1

After detection of the emission lines of NH_2CHO and HNCO toward MM1, we produced the integrated emission maps of the non-blended emission lines of those molecules by integrating the spectral data cubes using the channel ranges with the help of CASA task `IMMOMENTS`. The emission maps of NH_2CHO and HNCO toward MM1 are presented in Figure 3. The emission maps of NH_2CHO and HNCO are overlaid with a 988 μm continuum emission image of G358.93–0.03. The dust continuum image of G358.93–0.03 is taken from Manna et al. (2023). From the integrated emission maps, we observed that NH_2CHO and HNCO arose from the warm-inner regions of MM1. Since the excitation temperatures of NH_2CHO and HNCO toward MM1 are 165 ± 21 and 170 ± 32 K respectively, which indicates both molecules may exist in the same region of MM1, there is a high chance of a chemical link between NH_2CHO and HNCO toward MM1. We estimate the size of the emitting regions of NH_2CHO and HNCO by fitting 2D Gaussians over the emission maps of NH_2CHO and HNCO using the `IMFIT` task. The sizes of the emitting regions of NH_2CHO and HNCO corresponding to the non-blended transition lines are shown in Table 2. We observe that the emitting regions of NH_2CHO and HNCO are similar or marginally larger than the beam sizes of the emission maps. This suggests that the emission maps of NH_2CHO and HNCO are not spatially resolved or marginally resolved toward MM1. Therefore, we could not determine the chemical morphologies of NH_2CHO and HNCO from the integrated emission maps. Higher spatial and angular resolution observations are needed to learn the spatial distribution of NH_2CHO and HNCO toward MM1.

3.6. Searching for Other Peptide Bond Molecules Toward MM1

After the detection of the rotational emission lines of NH_2CHO and HNCO toward MM1, we also searched for the rotational emission lines of other COMs that have peptide bonds, such as $HOCH_2C(O)NH_2$, CH_3NCO, CH_3NHCHO, $NH_2C(O)CN$, CH_3CH_2NCO, $CH_3C(O)NH_2$, and $NH_2C(O)NH_2$ using the LTE modeled spectra. During the spectral analysis, we observed that all the above-mentioned molecules are blended with other molecular transitions. So, there is a very low chance of identifying these molecules. The upper-limit column densities of peptide bond molecules $HOCH_2C(O)NH_2$, CH_3NCO, CH_3NHCHO, $NH_2C(O)CN$, CH_3CH_2NCO, $CH_3C(O)NH_2$, and $NH_2C(O)NH_2$ are $\leqslant 3.56 \times 10^{14}\,cm^{-2}$, $\leqslant 8.26 \times 10^{14}\,cm^{-2}$, $\leqslant 5.20 \times 10^{13}\,cm^{-2}$,

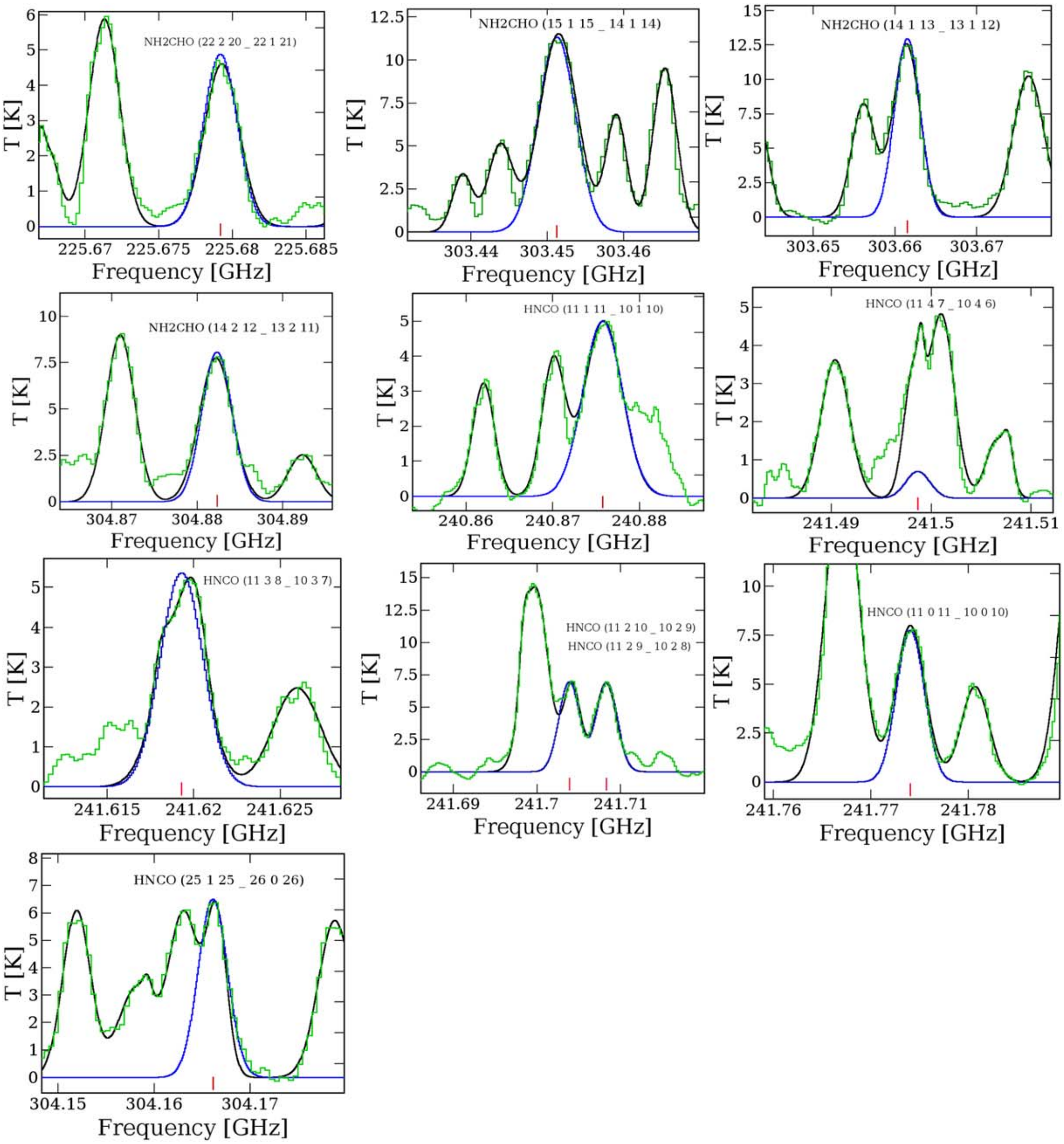

Figure 2. Emission lines of NH_2CHO and HNCO toward the MM1. The green lines represent the observed molecular spectra of MM1. The fitted blue spectra indicate the LTE-modeled spectra of NH_2CHO and HNCO. The fitted black spectra indicate the LTE-modeled spectra of other nearby molecules to understand the blended effect. The velocity of the spectra is -16.50 km s^{-1}.

$\leqslant 2.96 \times 10^{13}$ cm^{-2}, $\leqslant 9.62 \times 10^{13}$ cm^{-2}, $\leqslant 1.16 \times 10^{14}$ cm^{-2}, and $\leqslant 9.28 \times 10^{12}$ cm^{-2}, respectively.

4. Discussion

4.1. Comparison of the Abundances of NH_2CHO and HNCO Toward MM1 and Other Sources

To understand the distribution of NH_2CHO and HNCO in the ISM, we compare the fractional abundance of those molecules toward MM1 and other HMCs such as G10.47+0.03, G31.41+0.31, Orion KL, Sgr B2, and hot corino object IRAS 16293–2422 B. This comparison is presented in Table 3. After comparison, we noticed that the fractional abundance of NH_2CHO toward MM1 is quite similar to those of Sgr B2 and IRAS 16293–2422 B. The fractional abundance of NH_2CHO toward MM1 is one order of magnitude lower than those of G31.41+0.31, G10.47+0.03, and Orion KL. Similarly, the fractional abundance of HNCO toward MM1 is similar to those

Table 1
Molecular Line Properties of NH_2CHO and HNCO Toward the MM1

Molecule	Frequency (GHz)	Transition $(J'_{K'_aK'_c}$–$J''_{K''_aK''_c})$	E_u (K)	A_{ij} (s^{-1})	g_{up}	$S\mu^2$ (Debye^2)	FWHM (km s^{-1})	$\int T_{mb}dV$ (K km s^{-1})	Optical Depth (τ)	Remarks
NH_2CHO	225.679	22(2,20)–22(1,21)	275.80	3.20×10^{-5}	45	10.762	3.55 ± 0.82	13.57 ± 0.43	1.37×10^{-1}	Non blended
	303.451	15(1,15)–14(1,14)	120.01	2.05×10^{-3}	93	585.30	3.58 ± 0.29	44.61 ± 0.96	2.04×10^{-1}	Non blended
	303.661	14(1,13)–13(1,12)	113.00	2.04×10^{-3}	87	545.30	3.56 ± 0.37	42.71 ± 0.34	1.99×10^{-1}	Non blended
	304.882	14(2,12)–13(2,11)	120.54	2.04×10^{-3}	87	538.17	3.55 ± 0.44	27.44 ± 0.52	1.88×10^{-1}	Non blended
HNCO	240.875	11(1,11)–10(1,10)	112.64	1.90×10^{-4}	23	26.922	3.55 ± 0.62	20.56 ± 0.82	1.98×10^{-1}	Non blended
	241.498[a]	11(4,7)-10(4,6)	720.30	1.40×10^{-4}	23	19.679	⋯	⋯	1.04×10^{-2}	Blended with CHDCO
	241.619[a]	11(3,8)–10(3,7)	444.56	1.63×10^{-4}	23	22.877	3.58 ± 0.59	18.45 ± 0.34	8.55×10^{-2}	Non blended
	241.703[a]	11(2,10)–10(2,9)	239.89	1.81×10^{-4}	23	25.357	3.49 ± 0.21	15.28 ± 0.22	2.27×10^{-1}	Non blended
	241.708[a]	11(2,9)–10(2,8)	239.89	1.81×10^{-4}	23	25.356	3.48 ± 0.35	20.67 ± 0.61	2.37×10^{-1}	Non blended
	241.774	11(0,11)–10(0,10)	69.62	1.96×10^{-4}	23	27.458	3.52 ± 0.69	29.54 ± 0.87	5.69×10^{-1}	Non blended
	304.166	25(1,25)-26(0,26)	384.78	1.50×10^{-4}	51	23.34	3.55 ± 0.92	15.81 ± 0.21	1.13×10^{-1}	Non blended

Note.
[a] There are two transitions less than 100 kHz. We showed only the first transition.

Table 2
Emitting Regions of NH_2CHO and HNCO Toward the MM1

Molecule	Frequency (GHz)	Transition $(J'_{K'_aK'_c}$–$J''_{K''_aK''_c})$	E_{up} (K)	Emitting Region ($''$)
NH_2CHO	225.679	22(2,20)–22(1,21)	275.80	0.42
	303.451	15(1,15)–14(1,14)	120.01	0.43
	303.661	14(1,13)–13(1,12)	113.00	0.42
	304.882	14(2,12)–13(2,11)	120.54	0.43
HNCO	240.875	11(1,11)–10(1,10)	112.64	0.42
	241.619[a]	11(3,8)–10(3,7)	444.56	0.42
	241.703[a]	11(2,10)–10(2,9)	239.89	0.43
	241.708[a]	11(2,9)–10(2,8)	239.89	0.43
	241.774	11(0,11)–10(0,10)	69.62	0.43
	304.166	25(1,25)–26(0,26)	384.78	0.44

Note.
[a] There are two transitions within less than 100 kHz. We show only the first transition.

of Orion KL and Sgr B2. The fractional abundance of HNCO is one order of magnitude lower than that of G10.47+0.03 and G31.41+0.31. Furthermore, we notice that the fractional abundance of HNCO toward MM1 is two orders of magnitude larger than that of IRAS 16293–2422 B. Based on these comparisons, we identify that G31.41+0.31 and G10.47+0.03 are the most abundant NH_2CHO and HNCO sources in the ISM. The low abundances of NH_2CHO and HNCO toward MM1 indicate that the detection probabilities of other peptide bond COMs are very low in these sources.

4.2. Possible Formation Mechanism of NH_2CHO and HNCO Toward MM1

The formation mechanism(s) of NH_2CHO in ISM is still debatable in the astrochemistry community. We observed that only a few reactions have been proposed to understand the formation pathways of NH_2CHO in both the grain surface and gas phase. Previously, Quan & Herbst (2007) claimed that NH_2CHO is created via the ion-molecule reaction and subsequent electron recombination reaction between NH_4^+ and H_2CO

$$NH_4^+ + H_2CO \longrightarrow NH_3CHO^+ + H_2, \tag{1}$$

$$NH_3CHO^+ + e^- \longrightarrow NH_2CHO + H. \tag{2}$$

Subsequently, Garrod et al. (2008) pointed that the rates of reactions (1) and (2) are unknown. In particular, Garrod et al. (2008) proposed the following radical-neutral reaction in the gas phase

$$H_2CO + NH_2 \longrightarrow NH_2CHO + H. \tag{3}$$

However, Redondo et al. (2014) showed that the net activation barrier energy of this reaction is above 1000 K. Earlier, Garrod (2013) and Gorai et al. (2020) reported that reaction (3) is responsible for the formation of NH_2CHO toward HMCs and hot corinos. Previously Coutens et al. (2016) demonstrated that NH_2CHO was formed via the reaction between H_2CO and NH_2 (reaction (3)) in the gas phase toward the hot corino IRAS 16293–2422 B. Similarly, reaction (3) is also responsible for the formation of NH_2CHO in the shock region L1157–B1, hot cores Sgr B2 (N), G10.47+0.03, Orion KL, G31.41+0.31, and the high-mass protostar IRAS 18089–1732 (Halfen et al. 2011; Kahane et al. 2013; Codella et al. 2017; Gorai et al. 2020; Colzi et al. 2021; Manna et al. 2024).

Previous studies have proposed that the emission lines of HNCO originate from the high-density warm-inner regions of

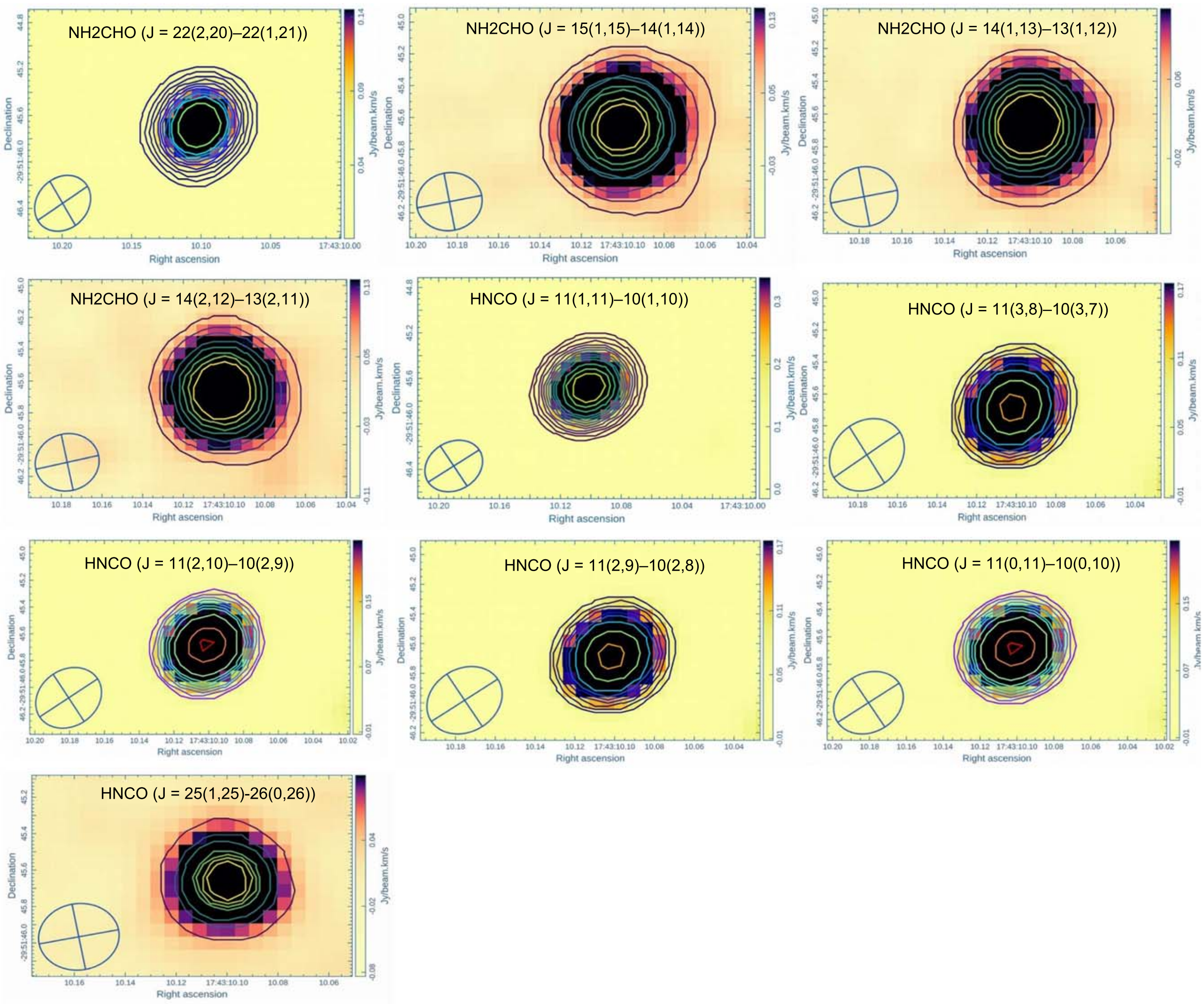

Figure 3. Emission maps of detected non-blended transitions of NH_2CHO and HNCO toward the MM1. The contours are the 988 μm continuum emission map of G358.93–0.03. The contour levels start at 3σ.

hot cores and hot corinos. Therefore, HNCO may play an important role as a tracer for dense gases in HMCs (Jackson et al. 1984). Previously, Iglesias (1977) claimed that HNCO is produced in the gas phase via the ion-neutral reaction toward Sgr B2

$$NCO^+ + H_2 \longrightarrow HNCO^+ + H, \tag{4}$$

$$HNCO^+ + H_2 \longrightarrow HNCOH^+ + H, \tag{5}$$

$$HNCOH^+ + e^- \longrightarrow HNCO + H. \tag{6}$$

Previously, Turner (2000) suggested another neutral-neutral reaction to create HNCO

$$CN + O_2 \longrightarrow NCO + O, \tag{7}$$

$$NCO + H_2 \longrightarrow HNCO + H. \tag{8}$$

Reaction (8) has an activation barrier. Previously, Garrod et al. (2008) showed that HNCO also is formed on the grain surface via the thermal reaction

$$NH + CO \longrightarrow HNCO. \tag{9}$$

Garrod et al. (2008) claimed that reaction (9) has no activation barrier and that the molecule is released in the gas phase via desorption. Earlier, Garrod (2013) and Gorai et al. (2020) showed that reaction (9) is the most efficient reaction for the formation of HNCO toward the HMCs.

Previously, Gorai et al. (2020) computed a three-phase (gas + grain + ice mantle) warm-up chemical model to understand the possible formation mechanisms of NH_2CHO and HNCO. During chemical modeling, they assumed the freefall collapse of a cloud (Phase I), which was followed by the warm-up phase (Phase II). In phase I, the density of the gas rapidly increased from 10^3 cm^{-3} to 1×10^7 cm^{-3} and the dust temperature was

Table 3
Comparison of the Abundances of NH_2CHO and HNCO Toward MM1 and Other Sources

Molecule	MM1[a]	G10.47+0.03[b]	G31.41+0.31[c]	Orion KL[d]	Sgr B2[e]	IRAS 16293–2422 B[f]
NH_2CHO	$(9.03 \pm 1.44) \times 10^{-10}$	2.87×10^{-9}	$(5.4 \pm 1.5) \times 10^{-9}$	5.80×10^{-9}	1.3×10^{-10}	1.05×10^{-10}
HNCO	$(5.80 \pm 2.09) \times 10^{-9}$	1.02×10^{-8}	$(1.1 \pm 0.3) \times 10^{-8}$	4.08×10^{-9}	7.20×10^{-9}	$(1.8 \pm 0.4) \times 10^{-11}$

Notes.
[a] Our work.
[b] Gorai et al. (2020).
[c] Colzi et al. (2021).
[d] Kahane et al. (2013), Tercero et al. (2010).
[e] Halfen et al. (2011), Adande et al. (2010).
[f] Kahane et al. (2013), Hernández-Gómez et al. (2019).

constant at 10 K. In phase II (the warm-up stage), the dust temperature was increased from 10 to 400 K, and the density of the gas was constant at 1×10^7 cm^{-3}. At this stage, the gas and dust in the hot core were well coupled. During chemical modeling, Gorai et al. (2020) used the radical-neutral reaction between H_2CO and NH_2 (reaction (3)) and the reaction between NH and CO (reaction (9)) for the formation of NH_2CHO and HNCO in the gas phase and grain surface, respectively. Previously, Garrod (2013) also demonstrated that reactions (3) and (9) are the most efficient for the formation of NH_2CHO and HNCO in the gas phase and grain surface toward HMCs. In the warm-up stage, Gorai et al. (2020) estimated the modeled abundances of NH_2CHO and HNCO toward HMCs to be 8.27×10^{-10} and 4.8×10^{-9}, respectively.

To understand the possible formation mechanism of NH_2CHO and HNCO toward MM1, we compared our derived abundance of NH_2CHO and HNCO with the modeled abundance of Gorai et al. (2020). This comparison is reasonable because the gas density and temperature of this source are 2×10^7 cm^{-3} and 150 K, respectively (Chen et al. 2020; Stecklum et al. 2021). Therefore, the three-phase warm-up chemical model of Gorai et al. (2020) is efficient for understanding the formation pathways of NH_2CHO and HNCO toward MM1. Gorai et al. (2020) derived the modeled abundance of NH_2CHO and HNCO to be 8.27×10^{-10} and 4.8×10^{-9}, respectively. The observed fractional abundances of NH_2CHO and HNCO toward MM1 are $(9.03 \pm 1.44) \times 10^{-10}$ and $(5.80 \pm 2.09) \times 10^{-9}$ respectively, which are quite similar to the modeled abundance results in Gorai et al. (2020). This result indicates that NH_2CHO is produced by the reaction of NH_2 and H_2CO in the gas phase toward MM1. Similarly, HNCO is created by the reaction of NH and CO on the surface of the grains of MM1.

4.3. *Chemical Link between NH_2CHO and HNCO*

Several studies have shown that NH_2CHO and HNCO are chemically connected. Earlier, Garrod et al. (2008), Haupa et al. (2019), and Gorai et al. (2020) claimed that the subsequent hydrogenation of HNCO creates NH_2CHO on the grain surface

$$\mathrm{HNCO + H \longrightarrow NH_2CO}, \tag{10}$$

$$\mathrm{NH_2CO + H \longrightarrow NH_2CHO}. \tag{11}$$

In another way, López-Sepulcre et al. (2015) demonstrated the molecular correlation between the abundance of HNCO and NH_2CHO toward the high-mass star formation regions. From the molecular correlation plot, López-Sepulcre et al. (2015) identified a positive correlation between the abundances of NH_2CHO and HNCO, and they found a correlation equation $X(\mathrm{NH_2CHO}) = 0.04X(\mathrm{HNCO})^{0.93}$ (see Figures 2 and 3 in López-Sepulcre et al. 2015). According to the molecular correlation equation of López-Sepulcre et al. (2015), we ascertained that the abundance of NH_2CHO is $(8.75 \pm 1.98) \times 10^{-10}$, which is very similar to our observed abundance of NH_2CHO toward MM1. This result indicates that HNCO and NH_2CHO are chemically connected toward MM1.

5. Conclusion

In this article, we present the identification of the emission lines of HNCO and NH_2CHO toward hot core MM1 using the ALMA bands 6 and 7. The conclusions of this study are summarized below:

1. We successfully detected four and six non-blended rotational transition lines of peptide bond molecules NH_2CHO and HNCO toward the hot core MM1.
2. The estimated column densities of NH_2CHO and HNCO toward the MM1 are $(2.80 \pm 0.29) \times 10^{15}$ cm^{-2} and $(1.80 \pm 0.42) \times 10^{16}$ cm^{-2} with excitation temperatures of 165 ± 21 K and 170 ± 32 K, respectively. The fractional abundances of NH_2CHO and HNCO toward MM1 are $(9.03 \pm 1.44) \times 10^{-10}$ and $(5.80 \pm 2.09) \times 10^{-9}$ respectively.
3. We compared the estimated abundances of NH_2CHO and HNCO with the existing three-phase warm-up chemical model abundances and noticed that the observed and modeled abundances are very close.

4. We claim that NH_2CHO is produced by the reaction of NH_2 and H_2CO in the gas phase toward MM1. Similarly, HNCO is created by the reaction of NH and CO on the grain surface of MM1.
5. We also discuss the chemical links between NH_2CHO and HNCO. According to the correlation equation of López-Sepulcre et al. (2015), both NH_2CHO and HNCO are chemically linked toward MM1. The presence of NH_2CHO and HNCO indicates that other O- and N-bearing molecules exist in this source, which we will discuss in follow-up studies.

Acknowledgments

We thank the anonymous referee for the helpful comments that improved the manuscript. A.M. acknowledges the SVMCM for financial support for this research. This paper makes use of the following ALMA data: ADS/JAO.ALMA#2019.1.00768.S and ADS/JAO.ALMA#2018.A.00031.T. ALMA is a partnership of ESO (representing its member states), NSF (USA), and NINS (Japan), together with NRC (Canada), MOST and ASIAA (Taiwan, China), and KASI (Republic of Korea), in co-operation with the Republic of Chile. The joint ALMA Observatory is operated by ESO, AUI/NRAO, and NAOJ.

Conflicts of Interest

The authors declare no conflict of interest.

ORCID iDs

Arijit Manna https://orcid.org/0000-0001-9133-3465
Sabyasachi Pal https://orcid.org/0000-0003-2325-8509

References

Adande, G. R., Halfen, D. T., Ziurys, L. M., Quan, D., & Herbst, E. 2010, ApJ, 725, 561
Adande, G. R., Woolf, N. J., & Ziurys, L. M. 2013, AsBio, 13, 439
Bayandina, O. S., Brogan, C. L., Burns, R. A., et al. 2022, AJ, 163, 83
Belloche, A., Müller, H. S. P., Menten, K. M., et al. 2013, A&A, 559, A47
Beuther, H., Churchwell, E. B., McKee, C. F., & Tan, J. C. 2007, Protostars and Planets V (Tucson, AZ: Univ. Arizona Press), 165
Bisschop, S. E., Jørgensen, J. K., Bourke, T. L., Bottinelli, S., & van Dishoeck, E. F. 2008, A&A, 488, 959
Bisschop, S. E., Jørgensen, J. K., van Dishoeck, E. F., et al. 2007, A&A, 465, 913
Biver, N., Bockelée-Morvan, D., Debout, V., et al. 2014, A&A, 566, L5
Blake, G. A., Sutton, E. C., Masson, C. R., & Phillips, T. G. 1987, ApJ, 315, 621
Brogan, C. L., Hunter, T. R., Towner, A. P. M., et al. 2019, ApJL, 881, L39
Bockelée-Morvan, D., Lis, D. C., Wink, J. E., et al. 2000, A&A, 353, 1101B
Colzi, L., Rivilla, V. M., Beltrán, M. T., et al. 2021, A&A, 653, A129
Codella, C., Ceccarelli, C., Caselli, P., et al. 2017, A&A, 605, L3
Chen, X., Sobolev, A. M., Ren, Z.-Y., et al. 2020, NatAs, 4, 1170
Churchwell, E., Wood, D., Myers, P. C., & Myers, R. V. 1986, ApJ, 305, 405
Coutens, A., Jørgensen, J. K., van der Wiel, M. H. D., et al. 2016, A&A, 590, L6
Canelo, C. M., Bronfman, L., Mendoza, E., et al. 2021, MNRAS, 504, 4428
Fedoseev, G., Ioppolo, S., Zhao, D., Lamberts, T., & Linnartz, H. 2015, MNRAS, 446, 439
Goesmann, F., Rosenbauer, H., Bredehöft, J. H., et al. 2015, Sci, 349, 020689
Gorai, P., Bhat, B., Sil, M., et al. 2020, ApJ, 895, 86
Garrod, R. T. 2013, ApJ, 765, 60
Garrod, R. T., Weaver, S. L. W., & Herbst, E. 2008, ApJ, 682, 283
Herbst, E., & van Dishoeck, E. F. 2009, ARA&A, 47, 427
Halfen, D. T., Ilyushin, V., & Ziurys, L. M. 2011, ApJ, 743, 60
Haupa, K. A., Tarczay, G., & Lee, Y.-P. 2019, JAChS, 141, 11614, JAChS
Hernández-Gómez, A., Sahnoun, E., Caux, E., et al. 2019, MNRAS, 483, 2014
Iglesias, E. 1977, ApJ, 218, 697
Jackson, J. M., Armstrong, J. T., & Barrett, A. H. 1984, ApJ, 280, 608
Kurland, R. J., & Wilson, E. B. 1957, JChPh, 27, 585
Kahane, C., Ceccarelli, C., Faure, A., & Caux, E. 2013, ApJL, 763, L38
Kukolich, S. G., Nelson, A. C., & Yamanashi, B. S. 1971, JAChS, 93, 6769
Kuan, Y., & Snyder, L. E. 1996, ApJ, 470, 981
López-Sepulcre, A., Jaber, A. A., Mendoza, E., et al. 2015, MNRAS, 449, 2438
Lapinov, A. V., Golubiatnikov, G. Y., Markov, V. N., & Guarnieri, A. 2007, AstL, 33, 121
Ligterink, N. F. W., Terwisscha van Scheltinga, J., Taquet, V., et al. 2018, MNRAS, 480, 3628
Mendoza, E., Lefloch, B., López-Sepulcre, A., et al. 2014, MNRAS, 445, 151
Muller, S., Beelen, A., Black, J. H., et al. 2013, A&A, 551, A109
MacDonald, G. H., Gibb, A. G., Habing, R. J., & Millar, T. J. 1996, A&AS, 119, 333
Manna, A., & Pal, S. 2022a, LSSR, 34, 9
Manna, A., & Pal, S. 2022b, JApA, 43, 83
Manna, A., & Pal, S. 2023, Ap&SS, 368, 33
Manna, A., & Pal, S. 2024, NewA, 109, 102199
Manna, A., Pal, S., Baug, T., & Mondal, S. 2024, RAA, 24, 065008
Manna, A., Pal, S., & Viti, S. 2024, MNRAS, submitted
Manna, A., Pal, S., Viti, S., & Sinha, S. 2023, MNRAS, 525, 2229
McMullin, J. P., Waters, B., Schiebel, D., Young, W., & Golap, K. 2007, in ASP Conf. Ser. 376, Astronomical Data Analysis Software and Systems XVI, ed. R. A. Shaw, F. Hill, & D. J. Bell (San Francisco, CA: ASP), 127
Müller, H. S. P., SchlMöder, F., Stutzki, J., & Winnewisser, G. 2005, JMoSt, 742, 215
Niedenhoff, M., Yamada, K. M. T., Belov, S. P., & Winnewisser, G. 1995, JMoSt, 174, 151
Perley, R. A., & Butler, B. J. 2017, ApJS, 230, 1538
Pickett, H. M., Poynte, R. L., Cohen, E. A., et al. 1998, JQSRT, 60, 883
Quan, D., & Herbst, E. 2007, A&A, 474, 521
Rubin, R. H., Swenson, G. W., Jr., Benson, R. C., Tigelaar, H. L., & Flygare, W. H. 1971, ApJL, 169, L39
Reid, M. J., Menten, K. M., Brunthaler, A., et al. 2014, ApJ, 783 130
Redondo, P., Barrientos, C., & Largo, A. 2014, ApJ, 780, 181
Saladino, R., Crestini, C., Pino, S., Costanzo, G., & Di Mauro, E. 2012, PhLRv, 9, 84
Snyder, L. E., & Buhl, D. 1972, ApJ, 177, 619
Stecklum, B., Wolf, V., Linz, H., et al. 2021, A&A, 646, A161
Turner, B. E. 2000, ApJ, 542, 837
Turner, B. E., Terzieva, R., & Herbst, E. 1999, ApJ, 518, 699
Tercero, B., Cernicharo, J., Pardo, J. R., & Goicoechea, J. R. 2010, A&A, 517, A96
van Dishoeck, E. F., & Blake, G. A. 1998, ARA&A, 36, 317
van Dishoeck, E. F., Blake, G. A., Jansen, D. J., & Groesbeck, T. D. 1995, ApJ, 447, 760
Vastel, C., Bottinelli, S., Caux, E., Glorian, J.-M., & Boiziot, M. 2015, CASSIS: A Tool to Visualize and Analyze Instrumental and Synthetic Spectra. in Proc. Annual Meeting of the French Society of Astronomy and Astrophysics, ed. F. Martins et al. (Toulouse: French Society of Astronomy and Astrophysics), 313
Williams, D. A., & Viti, S. 2014, Observational Molecular Astronomy: Exploring the Universe Using Molecular Line Emissions (Cambridge: Cambridge Univ. Press)
Yamaguchi, T., Takano, S., Watanabe, Y., et al. 2012, PASJ, 64, 105
Zinchenko, I., Henkel, C., & Mao, R. Q. 2000, A&A, 361, 1079